Detection of gas entrainment into liquid metals

T. Vogt [a,*], S. Boden [a], A. Andruszkiewicz [b], K. Eckert [c], S. Eckert [a], G. Gerbeth [a]

[a] Helmholtz-Zentrum Dresden-Rossendorf (HZDR), Institute of Fluid Dynamics, 01328 Dresden, Germany
[b] Faculty of Mechanical and Power Engineering, Wroclaw University of Technology, Poland
[c] Technische Universität Dresden, Institute of Fluid Mechanics, 01062 Dresden, Germany

HIGHLIGHTS

- We present liquid metal experiments dedicated to gas entrainment on the free surface.
- Ultrasonic and X-ray attenuation techniques have been used to study the mechanisms of gas entrainment.
- A comparison between bubbly flow in water and GaInSn showed substantial differences.
- Our results emphasize the importance of liquid metal experiments which are able to provide a suitable data base for numerical code validation.

ARTICLE INFO

ABSTRACT

Entrainment of cover gas into the liquid metal coolant is one of the principal safety issues in the design of innovative liquid metal-cooled fast reactors. We present generic experimental studies of this phenomenon in low-melting metals. Ultrasonic and X-ray diagnostic tools were considered for a visualization of gas entrainment at the free surface of the melt. Laboratory experiments were conducted using the eutectic alloy GaInSn, which is liquid at room temperature. Vortex-activated entrainment of air at the free surface of a rotating flow was revealed by ultrasonic techniques. X-ray radioscopy was used to visualize the behavior of argon bubbles inside a slit geometry. The measurements reveal distinct differences between water and GaInSn, especially with respect to the process of bubble formation and the coalescence and breakup of bubbles. Our results emphasize the importance of liquid metal experiments which are able to provide a suitable data base for numerical code validation.

1. Introduction

Controlling gas entrainment at the free surface of the liquid pool is one of the thermo-hydraulic challenges for operating liquid metal cooled fast reactors (Tenchine, 2010). The entrainment of a significant amount of cover gas by the liquid metal flow carries the risk that bursts of gas bubbles may run through the reactor core, causing a change in reactivity. Moreover, the occurrence of bubbles near the fuel rods impairs heat removal, or the gas may cause other operational problems, such as fluctuations in the pump discharge. Several mechanisms for bubble entrainment are possible in liquid metal cooled reactors (Baum and Cook, 1975; Madarame and Chiba, 1990): vortex activated entrainment, entrainment due to surface waves, and liquid fall entrainment. The main source of entrapped gas is the presence of either van-Karman vortices behind immersed structures or so-called "bathtub" vortices developing in rotating flows. A great deal of work has been conducted so far by many research groups to study the mechanisms of gas entrainment and identify efficient measures for mitigating this phenomenon (see, for instance, Banerjee and Padmakumar, 2009; Baum and Cook, 1975; Eguchi et al., 1994; Madarame and Chiba, 1990; Patwardhan et al., 2012; Satpathy et al., 2011; Yamaguchi et al., 2011). The majority of publications deal with numerical simulations and experimental studies using water models. Because of the lack of suitable measuring techniques, the number of experimental studies providing data from liquid metal flows is relatively low. However, new, innovative diagnostic tools based on ultrasonic, inductive and radiation techniques have been developed in the last decade, which enables effective studies of real liquid metal flows (Eckert et al., 2007, 2011).

In this paper we want to demonstrate the capabilities of ultrasonic techniques and X-ray radioscopy to detect gas entrainment at the free surface of liquid metal flows. We present two experiments here. The first considers a liquid metal flow that forms a tornado-like vortex with a funnel-shaped surface depression and

* Corresponding author. Tel.: +49 351 260 2451; fax: +49 351 260 12451.
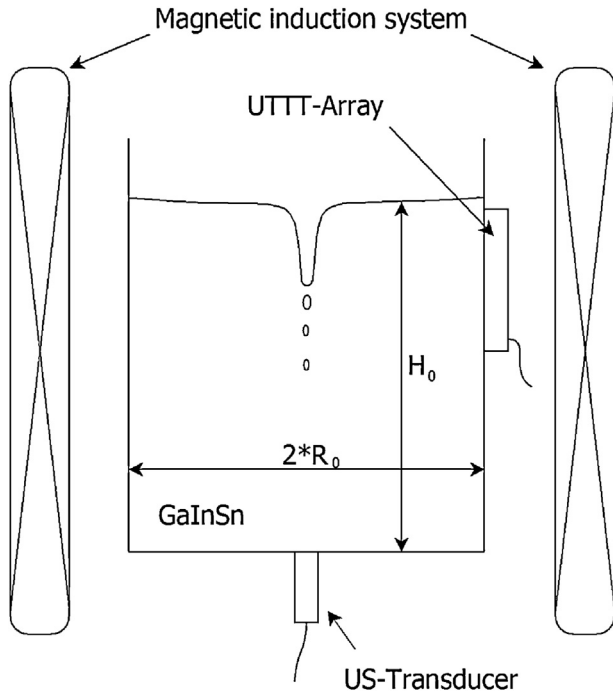E-mail address: t.vogt@hzdr.de (T. Vogt).

Fig. 1. Schematic drawing of the experimental setup.

incidental gas entrainment. Such vortex flows can be generated in liquid metals by the combined action of a rotating and a traveling magnetic field. The flow configuration is similar to that described in Vogt et al. (2013). Two different ultrasonic methods were used to track the position of the free surface and to detect gas bubbles entrapped inside the bulk liquid. Another experiment employs X-ray radioscopy to visualize rising gas bubbles in a rectangular box. The bubbles drive an intensive jet-like flow, which generates perturbations and waves at the free surface. The X-ray images show the entrainment of individual bubbles at outlying positions with respect to the bubble jet.

2. Vortex-induced gas entrainment

The spin-up of a concentrated, tornado-like vortex in a liquid metal bath was realized experimentally on a laboratory scale by using two independent magnetic body forces provided by a rotating magnetic field (RMF) and a vertically traveling magnetic field (TMF). The continuously applied RMF provides the source of angular momentum. A TMF pulse, about one order of magnitude stronger than the RMF, focuses this angular momentum toward the rotational axis and forms an intense, tornado-like vortex that induces gas entrainment at the bottom of this vortex funnel. The surface deformation and the gas entrainment into the liquid metal were observed by both the ultrasound Doppler method (Section 2.2) and the ultrasound transit-time-technique (UTTT, Section 2.3).

2.1. Experimental description

Fig. 1 shows a schematic drawing of the experimental setup. The experiments were carried out in the PERM magnetic induction system at Helmholtz-Zentrum Dresden-Rossendorf. The PERM stirrer provides a 200 mm bore and is designed to create a RMF with magnetic induction up to $B_R = 17$ mT and a TMF up to $B_T = 20$ mT. The actual magnetic induction applied in this experiment is on the order of $B_R \sim 1$ mT and $B_T \sim 10$ mT. The frequency of the RMF is $\omega_R/2\pi = 30$ Hz, while that of the TMF is $\omega_T/2\pi = 60$ Hz. These different frequencies were chosen in order to keep the interaction

between the RMF and TMF low. Two cylindrical vessels made of Perspex were placed alternatively in the middle of the 200 mm bore of the induction coils. The first cylinder had an inner diameter of $D_0 = 2 \times R_0 = 170$ mm and was filled up to a height of $H_0 = 170$ mm with the eutectic alloy GaInSn, which is liquid at room temperature. Material properties of the GaInSn alloy can be found in Plevachuk et al. (2014). The UTTT measurements require the attachment of a sensor array at the sidewall of the vessel. Because of the limited size of the induction system a smaller cylinder with an inner diameter of $D_0 = 90$ mm was used for that purpose and filled up to a height of $H_0 = 140$ mm. The free surface of the liquid metal in both cylinders was covered with a thin hydrochloric acid layer in order to avoid oxidation of the GaInSn alloy.

At the beginning of each measurement the liquid metal was set into a quasi-stationary swirling motion by the RMF. At time $t = 0$ s the rotating liquid metal is exposed to a strong, upwards-directed TMF. The following transient flow pattern is dominated by the formation of a tornado-like flow pattern along the rotational axis of the liquid metal. An example of the vortex funnel is shown in Fig. 2 The tornado can be clearly observed only during the first couple of seconds where the flow field is laminar and axisymmetric. After a few seconds, the flow becomes highly turbulent and the liquid metal tornado breaks down into turbulent spots. The vortex features mainly depend on the magnetic induction ratio of the TMF to the RMF. This ratio can be expressed in terms of non-dimensional parameters (F and Ta) as follows:

$$\frac{F}{Ta} = \frac{\omega_T}{\omega_R} * \frac{B_T^2}{B_R^2} * \frac{\kappa R_0}{2}$$

In this equation, ω_T and B_T stand for the frequency and amplitude of the TMF, respectively. Accordingly, ω_R and B_R denote the frequency and amplitude of the RMF. $\kappa = 21.8$ m^{-1} is the wave number of the TMF. The higher the F/Ta ratio, the deeper the tornados funnel. But also, the deeper the tornados funnel, the narrow it becomes. In addition to the force ratio F/Ta, the absolute value of F plays an important role as well. If F is sufficiently high (on the order of 10^{10}), bubbles are formed at the bottom of the vortex funnel. After their formation, the bubbles are dragged into the liquid since the liquid metal flows downwards along the axis of the vortex.

Immediately after the TMF is switched off, the bubbles emerge at the free surface (Fig. 3(b)) For a more detailed description of the underlying fluid dynamics, we refer to Vogt et al. (2013), since we will focus on the detection of the bubbles in this flow configuration.

2.2. Interface detection by ultrasound impulse echo technique

The surface deformation and the detection of the entrained bubbles were realized using a modified ultrasound Doppler velocimetry (UDV) system. The UDV technique is based on an impulse echo technique and is suitable for measuring instantaneous velocity profiles in opaque fluids. It was adopted by Takeda (1991) for experimental fluid dynamics. These days, ultrasound Doppler velocimetry has become an accepted measuring technique for flow investigations in various liquid metals such as mercury (Takeda et al., 1998), sodium (Eckert and Gerbeth, 2002) or alloys up to temperatures of about 700 °C (Eckert et al., 2003). In the present study, we used the DOP2000 velocimeter (model 2125, Signal Processing SA, Lausanne) equipped with a 4 MHz (TypeTR0411SS, acoustic active diameter 10 mm) transducer that was placed at the bottom wall of the vessel such that the ultrasonic beam coincides with the rotational axis of the cylindrical vessel. Instead of measuring fluid velocities, we used the UDV-device to detect the liquid metal interface by recording the ultrasound echo of the free surface and the echoes from the entrained gas bubbles. Therefore, the sensitivity of the UDV device was reduced significantly in order to
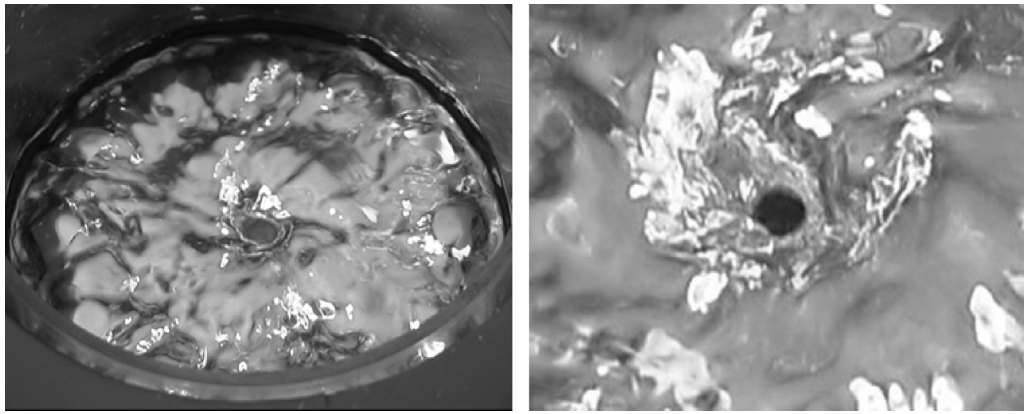
Fig. 2. Tornado-like vortex at the free surface of the melt.

blind out the echoes from microscopic particles, such as oxides. These weaker echoes can normally be used to determine the velocity distribution of the fluid along the beam line, but this is not of interest here. Instead, we recorded only the strong echoes from the interface between liquid metal and the bubbles.

Fig. 4 shows the result of the funnel depth detection. Fig. 4(a) depicts a measurement that was recorded at a rather low F/Ta ratio. The vertical axis in these contour plots represents the height of the vessel, and the abscissa is determined by the running time of the TMF. The instant $t = 0$ s corresponds to the moment where the TMF is switched on. The color scale represents the echo intensity associated with ultrasound bursts emitted from the ultrasound transducer that was placed at the bottom of the vessel. In Fig. 4(a), a very weak tornado can be observed with a maximum depth of approximately 20 mm at $t = 0.7$ s. The corresponding visual monitoring of the free surface by a video camera revealed a collapse of the tornado at about 1.2 s. The subsequent surface deformations are caused by turbulence.

Fig. 4(b) shows a measurement where the F/Ta ratio is significantly higher. The tornado funnel is formed at $t = 0.5$ s and collapses at approximately $t = 1.7$ s. The maximum funnel depth is about 30 mm. After the collapse of the tornado funnel, a lot of ultrasonic

echoes become visible below the free surface of the liquid metal at $H_0 = 170$ mm. These echoes are ultrasound waves which are reflected at bubbles entrapped in the liquid metal. Our experiments have shown two different stages of gas entrainment. During the first stage, air is sucked into the liquid metal at the bottom of the vortex funnel. This stage occurs at high F/Ta ratios when the vortex funnel is deep and thin. Fig. 5 shows a measurement at $F/Ta = 700$ where gas entrainment at the bottom of the tornado can be observed. The second stage of gas entrainment occurs abruptly at the moment when the vortex collapses. The gas entrained during the two stages of gas entrainment typically remains in the liquid metal as long as the TMF is turned on. Immediately after shutting down the TMF, a large number of gas bubbles can be observed at the free surface (Fig. 3(b)).

The interface detection by means of impulse echo detection works adequate if the interface covers the majority of the beam section. By contrast, in case of small bubbles or cavities, the echo intensity is relatively low. A detection of such weak echoes requires a higher amplification factor of the measuring device. As a result, the noise level becomes higher. A reliable distinction between cavities and measuring artifacts is therefore more difficult in such cases (see Fig. 5), but can be solved by a specific data processing.
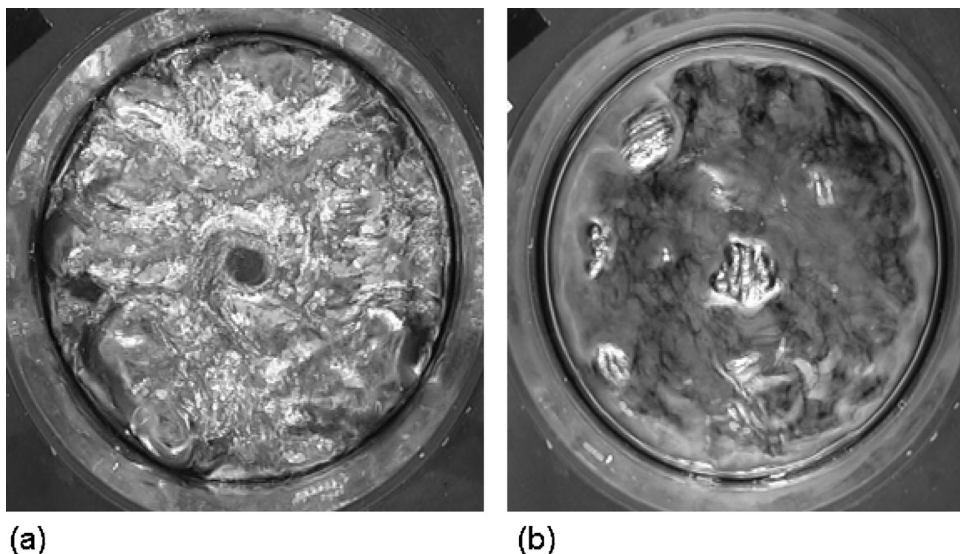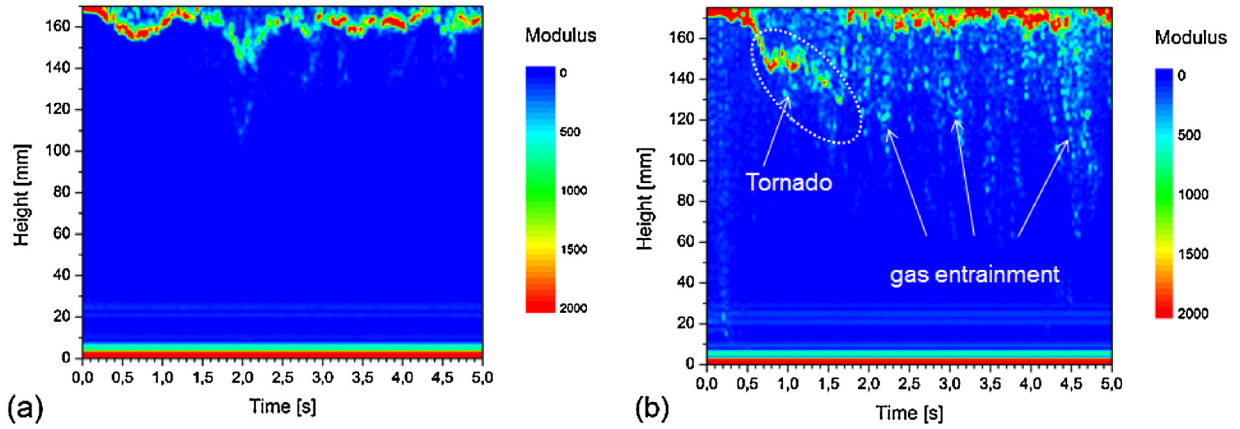

Fig. 3. Snapshots of the free surface of the melt: (a) forming of a liquid metal funnel; (b) emergence of gas bubbles at the free surface after the TMF shut-down. $F/Ta = 400$. Vessel dimension: $D_0 = 170$ mm; $H_0 = 170$ mm.

Fig. 4. Free surface detection by ultrasonic echo detection during the formation of the tornado-like vortex: (a) $F/Ta = 100$, $B_R = 2.71$ mT; $B_T = 14.1$ mT; (b) $F/Ta = 400$, $B_R = 1.36$ mT; $B_T = 14.1$ mT. Vessel dimension: $D_0 = 170$ mm; $H_0 = 170$ mm.

2.3. Bubble detection by means of ultrasound transit-time-technique

The gas entrainment of this flow configuration can alternatively be detected by the ultrasound transit-time-technique (Andruszkiewicz and Sommerlatt, 2008). In this approach, an ultrasound sensor array consisting of 10 ultrasound transducers was attached to the sidewall of the vessel (Fig. 1). The ultrasonic beams of the transducers run through the vessel at different heights. The sensor array is connected to an ultrasound defectoscope (USIP 40) loaded with the UltraPROOF software package (both from GE Inspection Technologies). The measuring technique uses the strong echoes from the interface between the two phases. If a bubble crosses the ultrasonic beam line, the measuring system detects a pronounced echo. The ultrasound transit-time between transducer and bubble can be determined, and the bubble position is calculated from that as described in Andruszkiewicz et al. (2013). The time resolution of the measuring system is about 2.5 ns. Because of its high temporal resolution, this technique is capable of tracking single bubbles. An example measurement of the UTTT is presented in Fig. 6. The diagram shows the ultrasonic transit times detected by each sensor in course of the experiment. The horizontal lines in this figure show the history of the echo intensity of each transducer. The vertical position of each transducer is given on the right-hand side of the figure, for which $z = 0$ mm corresponds to the filling height of the fluid. The measuring range is limited to $-0.9R_0 < r < 0.9R_0$ in order to blind out the strong interface echo from the vessel walls. If no bubble is within the ultrasonic beam, the respective transducer detects only weak echoes from the flow. These weak echoes, which are below a defined threshold value, are disregarded in this measurement (zero line). The detection of a bubble is indicated by the occurrence of distinct echo peaks along the respective measuring lines. Longer ultrasonic transit times correspond to larger distances between the sensor and the bubble position. The peaks at the upper three sensors are related to the tornado-like vortex funnel. At $t \approx 1$ s, one can observe the entrainment of a cavity at the bottom of the vortex funnel. This cavity is transported downwards with a speed of $u_z \approx -13$ cm/s and passes the lower transducer at $t \approx 1.3$ s. Between $1.7 < t < 2$ s one can observe a cavity traveling upwards with a speed $u_z \approx 40$ cm/s. Although not shown here, this measuring system also provides information about the radial position of the bubbles. Thus, the measuring system can also be utilized if the spatial distribution of bubbles over the cross-section of the vessel is of interest, as shown in Vogt et al. (2012).

3. X-ray visualization of gas bubbles in liquid metals

X-ray attenuation techniques can be used to visualize multiphase flows in opaque materials, in particular liquid metals. An X-ray radioscopic visualization method was used in the present study to investigate the behavior of a gas–liquid metal two-phase bubbly flow. The latter arises from a horizontal gas injection into a narrow liquid metal bubble column with rectangular cross-section. Dedicated software tools can calculate characteristic bubble quantities such as position, trajectory, size and velocity.

3.1. Experimental setup

A typical experimental setup used at HZDR is shown in Fig. 7(a). A Perspex container with parallel sidewalls and an rectangular inner cross-section of 200×12 mm^2 was filled with GaInSn up to a height of 300 mm. Argon gas is injected through two opposing cylindrical nozzles made from stainless steel, 30 mm above the container bottom. The inner and outer diameters of the nozzles were 0.5 mm and 4.0 mm, respectively. Argon gas flow rates through the nozzles were set independently by two mass flow controllers. The gas flow rate at each nozzle was varied between 100 and 3500 sccm (cm^3/min at norm conditions). The X-ray radioscopy setup used for visualization experiments is schematically depicted in Fig. 7(b). An X-ray tube produces a continuous X-ray beam that penetrates the liquid metal along the narrow extension of the container. The outgoing beam impinges on a scintillation screen where its intensity is
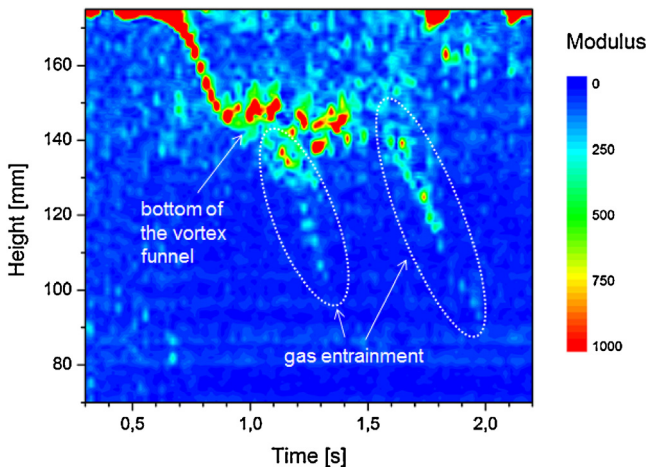
Fig. 5. Detection of gas entrainment at the bottom of the tornado funnel, $F/Ta = 700$, $B_R = 1$ mT; $B_T = 14.1$ mT. Vessel dimension: $D_0 = 170$ mm; $H_0 = 170$ mm.
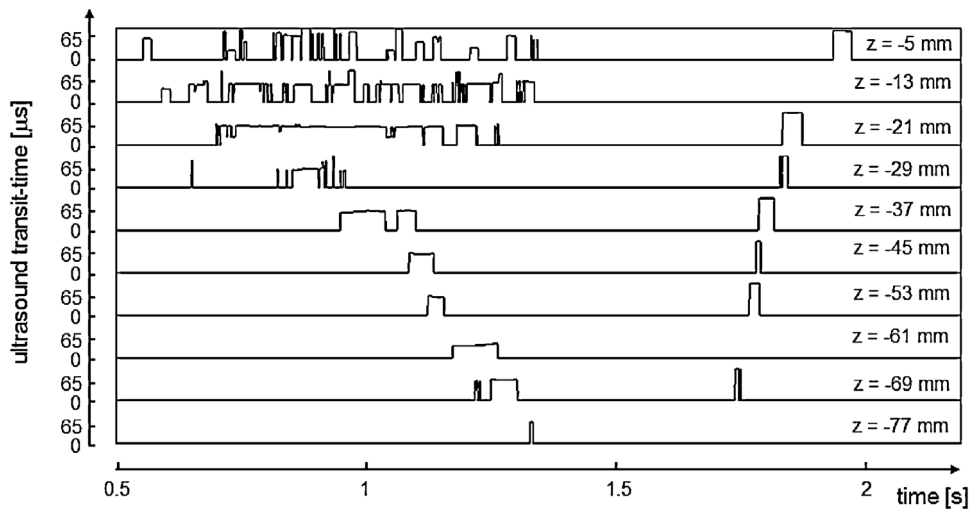
Fig. 6. Gas-entrainment at the bottom of the vortex funnel detected by ultrasound transit-time-technique via the sidewall of the vessel. $F/Ta = 320$, $B_R = 1$ mT; $B_T = 14.1$ mT. Vessel dimension: $D_0 = 90$ mm; $H_0 = 140$ mm.

converted into visible light which is deflected by a mirror and projected onto a CCD camera by a lens system. The distances between the X-ray source and the bubble column as well as between the scintillation screen and the optical system of the camera were varied to adjust different field of views (FOV). A shorter distance increases the signal to noise ratio but reduces the FOV. FOVs of 75×170 mm^2 and 200×150 mm^2 were used for visualization of the free surface of the liquid metal, the bubble plume and the entrainment of gas bubbles beneath the free surface.

### 3.2. Visualization of bubbly flows and gas entrainment at a strongly perturbed surface

The presentation of the experimental results will be started with a comparison between an argon-water and an argon-GaInSn flow. The initial experiments consider the effect of simultaneous gas injection at flow rates of 16.8 cm^3/s through both nozzles at the opposite sides of the fluid vessel (see Fig. 8). Fig. 8(a) shows a photograph under visible light source of argon-water flow and Fig. 8(b) shows an X-ray image of an argon-GaInSn flow. The two-sided gas injection creates a double-roll convection with an ascending flow in the bubble region near the sidewalls and a descending flow around the center of the container. The comparison between the water and

the liquid metal flow in Fig. 8 shows distinct differences concerning the internal structure of the bubbly flow. The considerably higher surface tension of GaInSn ($\sigma_S \sim 0.53$ N/m (Plevachuk et al., 2014)) provokes the formation of larger gas bubbles than those observed in water. The liquid metal flow shows a higher rate of bubble collision and subsequent coalescence. The rising bubbles in GaInSn ascend closer to the container sidewalls and have a perceptible effect on the global flow in the cell (representative flow measurements are not shown here).

Fig. 9 displays the region at the free surface which is heavily disturbed by the ascending gas bubbles. A multitude of small bubbles can be detected in the water (see Fig. 9(a)). The typical bubble size varies from 1 mm or less for the small bubbles beneath the free surface to about 10 mm for the rising gas bubbles. The application of high gas flow rates promotes a breakup of bubbles caused by high shearing forces and provokes foam formation just below the surface (see Fig. 9(a)). By contrast, the shape of the liquid metal surface is smoother at the same gas flow rate (see Fig. 9(b)). Obviously, very few smaller gas bubbles can be detected here which can be explained by the dramatic difference in the surface tension. In other words, much more energy has to be spent in liquid metals to increase the interfacial area to produce many small gas bubbles. These facts allow drawing the conclusion that the probability for
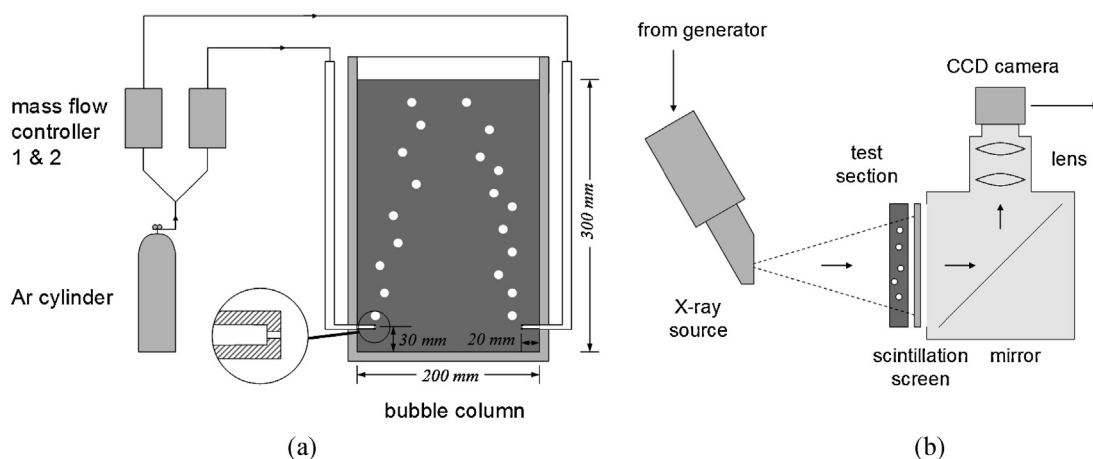
Fig. 7. Experimental setup: (a) sketch of the two-phase flow experiment (the narrow side of 12 mm was along the X-ray beam); (b) schematic view of the X-ray radioscopy setup.
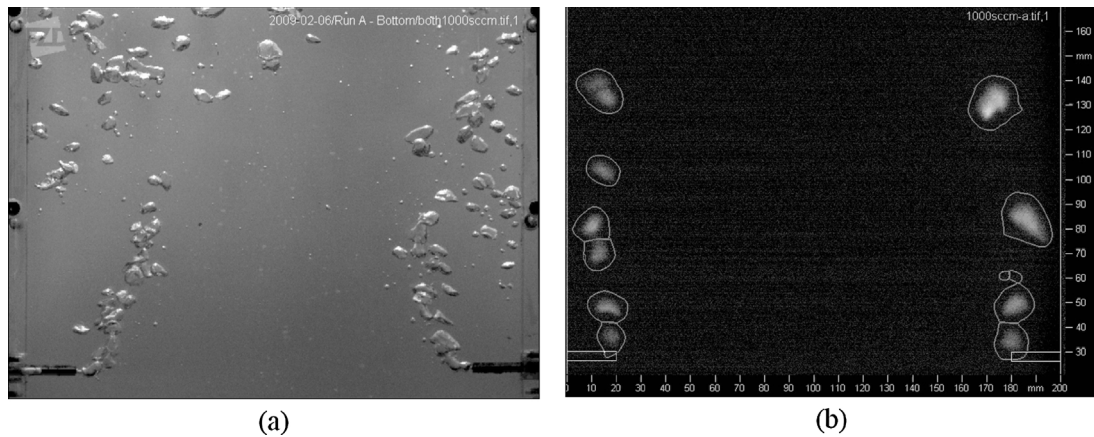
Fig. 8. Snapshots showing the bubbly flow resulting from a simultaneous gas injection through both nozzles (Q_g = 16.8 cm^3/s): (a) argon-water; (b) argon-GaInSn. The size of the FOV is given by the scale in (b).

gas entrainment in water must be higher as for liquid metal under comparable flow conditions.

Further experiments were focused on the detection of bubble entrainment at the liquid metal surface. Fig. 10 contains a sequence of four X-ray images showing the occurrence of gas entrainment triggered by a bubble-induced violation of the free surface. The density distribution inside the fluid container is represented by a false color image here. Regions covered by the liquid metal appear as blue areas. The void zones and argon bubbles are depicted in red and yellow, respectively, whereas yellow corresponds to lower void fraction. The ascending gas bubbles reach the free surface close to the sidewalls on the right of the images. High gas flow rates generate a strong ascending flow that is redirected near the free surface, which is associated with large deflections of the surface (Fig. 10(a)). In this way, a stronger circulating flow is generated below the surface as shown in Fig. 10(b). A formation of bubbles can be observed at positions where indentations of the free surface occur (see the white circle in Fig. 10(c)). A sufficiently high shear stress sucks small bubbles from the free surface into the bulk and breaks up larger bubbles just below the free surface. The bubbles are transported downwards by the circulating fluid flow.

Our observations revealed that these gas bubbles remain entrapped in the vortex region for a rather long time, see Fig. 10(d) in which examples of trapped argon bubbles are marked by white circles. Residence times of such bubbles within the field of view were on the order of tens of seconds, which is much longer than the time needed for bubbles to rise from the nozzle to the surface.

An increase in the injected gas flow rate results in higher surface velocities and an increase in the frequency of bubble entrainment. A larger number of bubbles trapped within the recirculating vortex below the free surface enhance the probability of bubble coalescence. The coalescent bubbles show a reduced residence time inside the liquid metal.

4. Summary

The present paper demonstrates the phenomenon of gas bubble entrainment at the free surface of a liquid metal in small-scale experiments using the low-melting alloy GaInSn as a model fluid. Ultrasonic and X-ray attenuation techniques have been used to study the mechanisms of bubble entrainment. A comparison between bubbly flow in water and GaInSn showed substantial differences in the process of bubble formation, motion, coalescence, breakup, etc. Such findings confirm the importance of suitable liquid metal model experiments as a tool for gaining an advanced understanding of liquid metal two-phase flows and gas entrainment processes.

One of the series of experiments considers the transient, tornado-like flow structure arising from a TMF spin-up in a rotating liquid metal. The aim of the measurements was to monitor the free surface deformation and the detection of gas entrainment at the bottom of the vortex funnel. For this reason, an adapted ultrasonic echo technique was used to detect the surface position. Furthermore, this measuring approach was able to
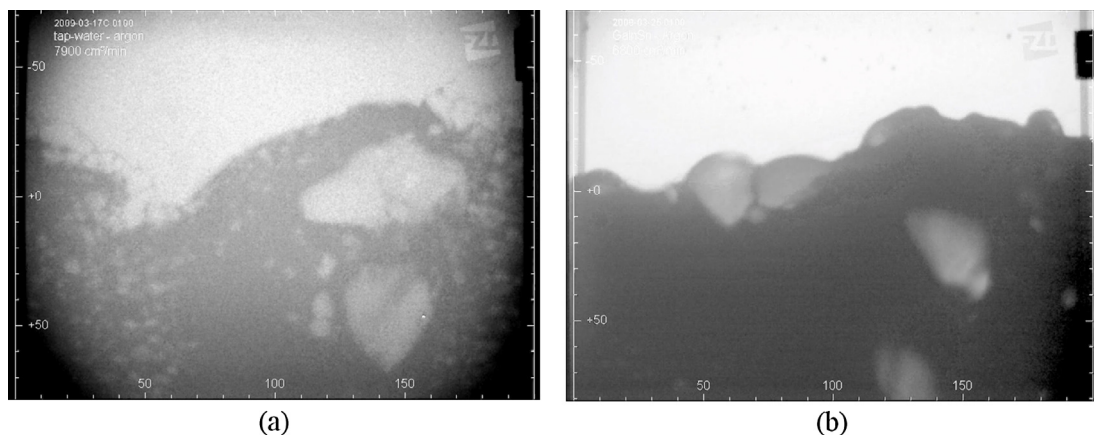
Fig. 9. Snapshots showing the free surface of the melt perturbed by the ascending bubbles: (a) argon-water (Q_g = 131.7 cm^3/s); (b) argon-GaInSn (Q_g = 113.3 cm^3/s). The size of the images is 200 × 150 mm^2.
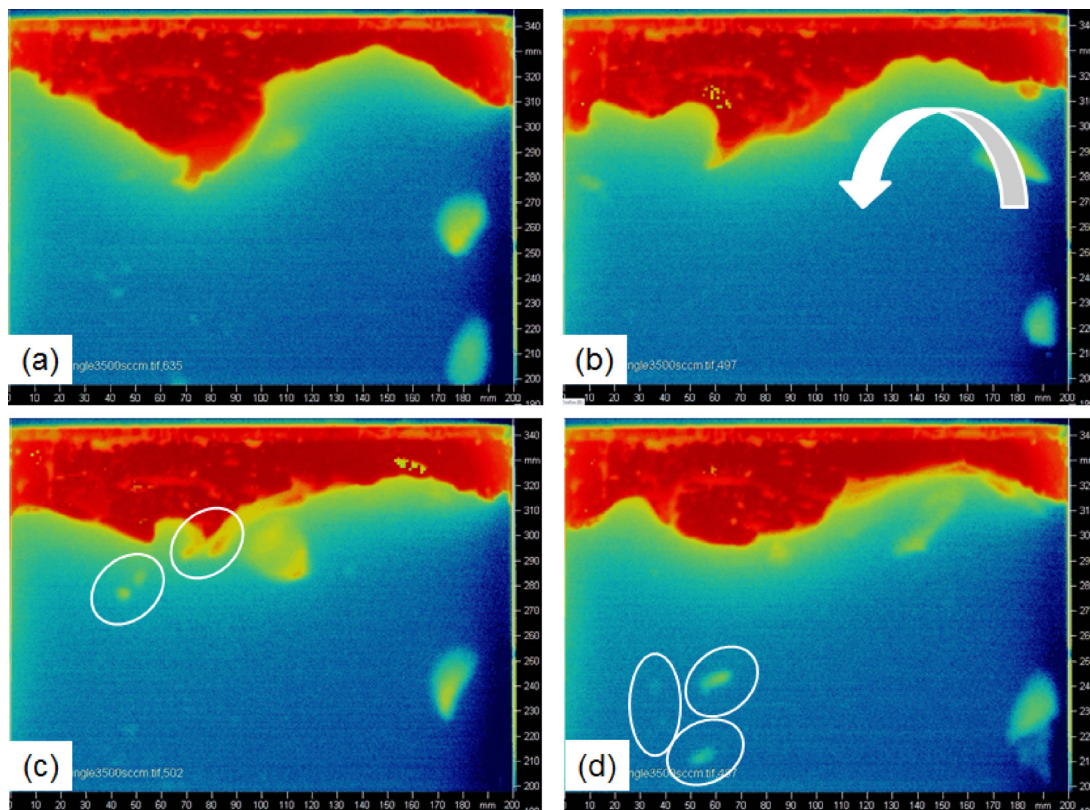
Fig. 10. Sequence of X-ray images showing the process of bubble entrainment at the strongly perturbed free surface of the liquid metal (see online version of this article for color coded version of this figure)

observe gas entrainment into the liquid metal. This gas entrainment was found to occur in two ways: first at the bottom of the tornado funnel and second, at greater depth from the interface at the moment when the tornado collapses.

The gas entrainment at the vortex flow configuration was alternatively detected by the ultrasound transit time technique from the vessel sidewall. This technique uses an ultrasound array and short pulses to detect the bubbles inside the liquid metal. Due to the high temporal resolution of this measuring system, even single bubbles with high velocities can be tracked throughout the volume.

X-ray visualization applied within this study gives a clear and impressive picture of the gas-liquid metal two-phase flow in a flat, rectangular container. Several image processing techniques provide essential characteristics of the bubbly flow such as bubble position, velocities and size. Gas entrainment was observed to result from strong perturbations of the liquid metal surface. Further measurements are planned for liquid sodium as part of the upcoming DRESDYN project at HZDR (Stefani et al., 2012). The lower density of liquid sodium compared with GaInSn allows these experiments to be performed in larger experimental volumes. Furthermore, we will consider an application of ultrafast X-ray tomography (Hampel et al., 2005) in liquid sodium. This technique offers a very attractive possibility for a three-dimensional reconstruction of the gas-liquid interfacial structure of bubbly flows in liquid metals.

All in all, it is not possible to model the behavior of liquid metal bubbly flows accurately by means of experiments in water owing to the discrepancies in the material properties. There is still a shortage of reliable experiments in liquid metals because of the challenges to measure the flow quantities with reasonable accuracy and resolution. The ultrasonic techniques and the X-ray radioscopy do not offer a final solution of this problem, but, may open the door for performing liquid metal two phase flow experiments in the context of liquid metal cooled fast reactors development which can deliver a valuable data base for code validation.

Acknowledgements

References

Andruszkiewicz, A., Sommerlatt, H., 2008. Ultrasonic measurements of flow in two-phase liquid–gas systems. Part I: the method for measurements. Chem. Process Eng. 29, 113–128.

Andruszkiewicz, A., Eckert, K., Eckert, S., Odenbach, S., 2013. Gas bubble detection in liquid metals by means of the ultrasound transit-time-technique. Eur. Phys. J. Spec. Top. 220, 53–62.

Banerjee, I., Padmakumar, G., 2009. Mitigation of Gas Entrainment for Prototype Fast Breeder Reactor. IGCAR Engineering.

Baum, M.R., Cook, M.E., 1975. Gas entrainment at the free surface of a liquid: entrainment inception at a vortex with an unstable gas core. Nucl. Eng. Des. 32, 239–245.

Eckert, S., Gerbeth, G., 2002. Velocity measurements in liquid sodium by means of ultrasound Doppler velocimetry. Exp. Fluids 32, 542–546.

Eckert, S., Gerbeth, G., Melnikov, V.I., 2003. Velocity measurements at high temperatures by ultrasound velocimetry using an acoustic wave guide. Exp. Fluids 35, 381–388.

Eckert, S., Cramer, A., Gerbeth, G., 2007. Velocity measurement techniques for liquid metal flows. In: Molokov, S. (Ed.), Magnetohydrodynamics – Historical Evolution and Trends. Springer, pp. 275–294.

Eckert, S., Buchenau, D., Gerbeth, G., 2011. Some recent developments in the field of measuring techniques and instrumentation for liquid metal flows. J. Nucl. Sci. Technol. 48, 490–498.

Eguchi, Y., Yamamoto, K., Funada, T., Tanaka, N., Moriya, S., Tanimoto, K., Ogura, K., Suzuki, T., Maekawa, I., 1994. Gas entrainment in the IHX vessel of top-entry loop-type LMFBR. Nucl. Eng. Des. 146, 373–381.

Hampel, U., Speck, M., Koch, D., Menz, H.J., Mayer, H.G., Fietz, J., Hoppe, D., Schleicher, E., Zippe, C., Prasser, H.M., 2005. Ultrafast X-ray computed tomography with a linearly scanned electron beam source. Flow Meas. Instrum. 16, 65–72.

Madarame, H., Chiba, T., 1990. Gas entrainment inception at the border of a flow-swollen liquid surface. Nucl. Eng. Des. 120, 193–201.

Patwardhan, A.W., Mali, R.G., Jashao, S.B., Bhor, K.D., Padmakumar, G., Vaidyanathan, G., 2012. Argon entrainment into liquid sodium in fast breeder reactor. Nucl. Eng. Des. 249, 204–211.

Plevachuk, Y., Sklyarchuk, V., Eckert, S., Gerbeth, G., Novakovic, R., 2014. Thermo-physical properties of the liquid Ga–In–Sn eutectic alloy. J. Chem. Eng. Data 59, 757–763.

Satpathy, K., Velusamy, K., Chellapandi, P., 2011. Computational fluid dynamic studies on gas entrainment in fast breeder reactors. Energy Procedia 7, 333–339.

Stefani, F., Eckert, S., Gerbeth, G., Giesecke, A., Gundrum, Th., Steglich, C., Weier, T., Wustmann, B., 2012. DRESDYN – a new facility for MHD experiments with liquid sodium. Magnetohydrodynamics 48, 103–113.

Takeda, Y., 1991. Development of an ultrasound velocity profile monitor. Nucl. Eng. Des. 126, 277–284.

Takeda, Y., Kikura, H., Bauer, G., 1998. Flow measurement in a SINQ mockup target using mercury. In: Proc. of ASME FED Summer Meeting, ASME, Washington, DC.

Tenchine, D., 2010. Some thermal hydraulic challenges in sodium cooled fast reactors. Nucl. Eng. Des. 240, 1195–1214.

Vogt, T., Andruszkiewicz, A., Eckert, S., Eckert, K., Odenbach, S., Gerbeth, G., 2012. Mixing enhancement in gas-stirred melts by rotating magnetic fields. Metall. Mater. Trans. B, 1454–1464.

Vogt, T., Grants, I., Eckert, S., Gerbeth, G., 2013. Spin-up of a magnetically driven tornado-like vortex. J. Fluid Mech. 736, 641–662.

Yamaguchi, A., Tatsumi, E., Takata, T., Ito, K., Ohshima, H., Kamide, H., Sakakibara, J., 2011. Gas entrainment allowance level at free surface and gas dynamic behavior of sodium-cooled fast reactor. Nucl. Eng. Des. 241, 1627–1635.